



Silica-supported Cu₂O nanoparticles with tunable size for sustainable hydrogen generation

Gang Wang^a, Roy van den Berg^a, Celso de Mello Donega^b, Krijn P. de Jong^a,
Petra E. de Jongh^{a,*}

^a Inorganic Chemistry and Catalysis, Debye Institute for Nanomaterials Science, Utrecht University, Utrecht, The Netherlands

^b Condensed Matter and Interfaces, Debye Institute for Nanomaterials Science, Utrecht University, Utrecht, The Netherlands



ARTICLE INFO

Article history:

Received 9 January 2016
Received in revised form 17 March 2016
Accepted 21 March 2016
Available online 24 March 2016

Keywords:

Cuprous oxide
Mesoporous silica
Crystallite size
Band gap
Hydrogen generation

ABSTRACT

Cu₂O is a p-type semiconductor which attracts much attention for application in photovoltaics, photocatalysis and solar water splitting. However, Cu₂O is not intrinsically stable under illumination in aqueous solutions, and the edge of the valence band is not positive enough to provide sufficient overpotential for water oxidation. The stability and band edge position of nanostructured materials depend on crystallite size. In this paper, we describe a new strategy to vary the size of Cu₂O nanoparticles using mesoporous silica supports. First, CuO nanoparticles were obtained via impregnation-drying-heating. The size of the nanoparticles was tuned by varying either the concentration of Cu precursor or the pore diameter of the supporting silica. Subsequently, the CuO was converted to Cu₂O without particle growth by gas-phase reduction with carbon monoxide. The visible light absorption of these nanoparticles depended on the copper oxide phase and crystallite size, leading to a direct band gap energy of 2.60 eV for 2 nm Cu₂O nanoparticles compared to 1.94 eV for macrocrystalline Cu₂O. Our results highlight a new synthesis strategy for the preparation of metal-oxide nanoparticles with controlled sizes of 2–15 nm that are not directly accessible by alternative synthesis techniques. The as-obtained 15 nm Cu₂O nanoparticles were used for H₂ evolution in a water-methanol mixture, the photocatalyst gave a H₂ evolution rate of $11.5 \times 10^{-3} \mu\text{mol min}^{-1}$ which corresponded to an internal quantum efficiency of 15.8% and an overall quantum efficiency of 3.5% for light between 310 and 710 nm. Finally, the nanoparticles were stable during three hours of light illumination.

© 2016 Elsevier B.V. All rights reserved.

1. Introduction

Since Honda and Fujishima's proof of principle for photoelectrochemical water splitting using TiO₂, several metal oxide semiconductors such as TiO₂, Ta₂O₅, and ZrO₂ have been proposed in the past decade as promising materials for water splitting [1–3]. However, these materials do not absorb visible light as their band gap is larger than 3.1 eV, so they cannot absorb sunlight efficiently. Cuprous oxide (Cu₂O) is a p-type semiconductor with a band gap energy of 2.0–2.2 eV [4,5], ideally suited for solar energy conversion and hydrogen evolution from water. Hara et al. showed that Cu₂O can be used as a photocatalyst for overall water splitting under visible light irradiation, the quantum efficiency of the photocatalytic reaction was estimated at ca. 0.3% between 550 and 600 nm [6]. Copper oxide materials are readily available, and the

conduction band edge of Cu₂O (ca. –0.74 V vs. NHE) is sufficiently more negative than the reduction potential of water (0 V vs. NHE) [7]. However, there is little overpotential available for oxygen evolution because the valence band edge of Cu₂O (ca. +1.26 V vs. NHE) is close to the oxidation potential of water (ca. +1.23 V vs. NHE) [7]. Furthermore, under illumination Cu₂O can undergo photodegradation in aqueous solutions [6], either being reduced to metallic copper (Cu) or being oxidized to Cu²⁺ because the redox potentials of both the reduction and oxidation of Cu₂O lie within its bandgap [7]. A possible strategy to increase the stability of Cu₂O is to limit the direct contact between Cu₂O and solution by depositing a protective thin film of carbon or wide band gap semiconducting oxides, such as TiO₂ [8,9].

For several reasons, it would be very interesting to study Cu₂O nanoparticles with different sizes. Firstly, nanoscale Cu₂O is postulated to be more stable than bulk Cu₂O, and parameters such as the crystallite size and crystal facets seem to play an important role in increasing the intrinsic stability of Cu₂O [10]. Secondly, the band gap of the metal oxide semiconductor depends on the

* Corresponding author.

E-mail address: P.E.deJongh@uu.nl (P.E. de Jongh).

crystallite size, and it is an interesting question how the position of the valence band is affected. On the other hand, recombination rates might be increased for small particles [11]. It will be very valuable to develop a controlled synthesis method for well-defined supported Cu₂O nanoparticles with variable particle size, to allow investigation of these issues.

Various Cu₂O nanoparticles such as cubes, octahedral, nanowire and hollow structures have been synthesized by colloidal methods [12,13]. However, it is hard to control the reaction towards complete Cu₂O formation without the generation of Cu or CuO, and difficult to remove the attached ligands, while it would be interesting to study ligand-free catalysts. It is possible to obtain Cu₂O by oxidation of Cu or reduction of CuO. Several research groups have already investigated the preparation of silica supported Cu and CuO nanoparticles. It was reported by Gallo et al. that silica supported copper nanoparticles with tunable size were obtained by selective step-wise chemical vapor deposition and decomposition, using bis-(hexafluoroacetylacetone) copper(II) hydrate as a precursor [14]. Touponce et al. also showed that the sizes of silica supported Cu and CuO nanoparticles were influenced by the experiment conditions, they managed to tune the particle size between 2.5 nm and 40 nm by changing the nature of the copper precursor, the copper content, and the thermal treatments when using incipient wetness impregnation for catalyst preparation [15]. Recent research in our group has also shown great progress in the control over size and location of silica supported Cu and CuO nanoparticles [16,17]. The stability of these supported nanoparticles as catalysts operating under dynamic conditions depends on the spatial distribution over the support materials [18,19]. Building on skills and methods from the field of supported catalysts [20], we demonstrate a new strategy to prepare small (<20 nm) Cu₂O nanoparticles, starting from mesoporous silica supported Cu or CuO nanocrystallites, which are converted into Cu₂O without any significant change in crystallite size.

Different types of ordered mesoporous silica were used as supporting materials in this research. Mesocellular foam (MCF) is a mesoporous silica with a 3-D pore system comprising large spherical cages interconnected by windows [21]. SBA-15 is an ordered mesoporous silica comprising uniform pores that can be tuned between 5 and 15 nm diameter with a narrow pore size distribution [22]. SBA-16 is a highly ordered 3-D porous silica with cage-like mesopores [23]. MCM-41 consists of a highly ordered 2-D cylindrical mesopore system [24].

2. Experimental

All chemicals were purchased from Sigma–Aldrich unless otherwise stated.

2.1. Silica supports

The preparation methods of mesoporous silica were as follows: (1) MCF: 4.0 g of triblock copolymer Pluronic P123 was added to a mixture of 130 mL of water and 20 mL of 37% HCl aqueous solution in a 500 mL polypropylene bottle, which was stirred overnight at room temperature. After that, 4 g of 1,3,5-trimethylbenzene (TMB) was added dropwise and stirred for 4 h. Then 8.5 g of tetraethyl orthosilicate (TEOS) was added to this solution under vigorous stirring. After 5 min of stirring, the mixture was kept under static conditions for 20 h at 39 °C, then 46 mg of ammonium fluoride (NH₄F) was added under stirring, followed by 24 h hydrothermal treatment at 90 °C. The solid products were collected by filtration, washed with water, dried, and calcined in static air for 6 h at 550 °C [21].

(2) SBA-15: 4.0 g of triblock copolymer Pluronic P123 was added to a mixture of 130 mL of water and 20 mL of 37% HCl aqueous solution in a 500 mL polypropylene bottle, which was stirred overnight at room temperature. Then, 8.5 g of TEOS was added to this solution under vigorous stirring. After 5 min of stirring, the mixture was kept under static conditions for 20 h at 39 °C, followed by 24 h hydrothermal treatment at 80 °C. The solid products were collected by filtration, washed with water, dried, and calcined in static air for 6 h at 550 °C [22].

(3) SBA-16: 3.0 g of Pluronic F127 copolymer (EO₁₀₆PO₇₀EO₁₀₆) was added to a mixture of 144 mL of water and 5 mL of 37% HCl aqueous solution in a 500 mL polypropylene bottle, which was stirred overnight at room temperature. Then, 9.0 g of 1-butanol was added to this solution dropwise. After 1.5 h of stirring, 14.2 g of TEOS was added under vigorous stirring. After 5 min of stirring, the mixture was kept under static conditions for 24 h at 40 °C, followed by 24 h hydrothermal treatment at 80 °C. The solid products were collected by filtration, washed with water, dried, and calcined in static air for 6 h at 550 °C [23].

(4) MCM-41: 3.5 mL of NaOH (2 M) solution was mixed with 480 mL of distilled water. Then 1.0 g of hexadecyltrimethylammonium bromide (CTAB) was added to the solution under stirring at 80 °C for 2 h. After that, 5 mL of TEOS was dropped in slowly, giving rise to a white slurry, the solution was stirred for another 2 h, the resulting product was filtered, washed with distilled water, dried at ambient temperature, followed by calcination in static air for 4 h at 550 °C [24].

Aside from ordered mesoporous silica, Aerosil 300 and commercially available silica gels with different pore sizes (3 nm, 6 nm, 15 nm, 23 nm, received from Grace Co.) were also used.

2.2. Nanoparticles@Silica

Silica supported nanoparticles were prepared via incipient wetness impregnation followed by drying and heat treatment. Typically, 500 mg of dry mesoporous silica scaffolds were impregnated under vacuum with different concentrations (from 0.375 M to 2.955 M) of Cu(NO₃)₂·3H₂O in 0.1 M HNO₃ aqueous solutions. The volume of the solution used for the impregnation corresponded to the total pore volume of the support that was impregnated (incipient wetness impregnation). The sample was dried under vacuum overnight at room temperature, and then transferred to a tubular reactor, where the sample was heated to 350 °C (2 °C/min) under 375 mL/min of 2% NO/98% N₂ gas flow [16] and kept at this temperature for 3 h, yielding supported CuO nanocrystallites.

Supported Cu nanocrystallites were prepared as follows: 100 mg of the as-obtained CuO nanocrystallites were transferred into a tubular reactor which connected with a 30 mL/min of 20% H₂/80% N₂ gas flow. The samples were heated to 250 °C with a temperature ramp of 2 °C/min, and kept at this temperature for 3 h. After the reduction treatment the resulting Cu/SiO₂ was passivated in air at room temperature for 5 min. The sample was stored in a glove box under argon atmosphere.

To obtain Cu₂O from metallic copper (Cu) by oxidation, 100 mg of silica supported Cu was dispersed into 50 mL chloroform and stirred under ambient conditions for 24 h. The solid products were collected by filtration, washed with water and dried under vacuum. To reduce CuO to Cu₂O, both isothermal and gradient methods were investigated. 100 mg of the silica-supported CuO was transferred into a tubular reactor, and reduced under 20 mL/min 5% CO/95% N₂ gas flow at 250 °C for different times. Alternatively, the samples were heated to 250 °C at a rate of 5 °C/min under 50 mL/min of 5% H₂/95% Ar gas flow.

Supported CuO and Cu samples are denoted Cu(O)·X·Y, where X is the silica type, Y is the weight loading of Cu; Supported Cu₂O samples are denoted X·Y·Z, where Z indicates the strategy of obtaining

Table 1

Overview of samples designation and their copper content.

sample name (after CO/H ₂ /CH ₃ Cl)	sample name of Cu(O)	silica support	average pore size (nm)	weight loading of Cu (%)	strategy to obtain Cu ₂ O
ARS_10.0_CH	Cu.ARS_10.0	Aerosil 300	3	10.0	oxidation in chloroform
ARS_10.0_CO	CuO.ARS_10.0	Aerosil 300	3	10.0	CO reduction
MCF_18.7_CH	Cu.MCF.18.7	MCF	30	18.7	oxidation in chloroform
MCF_6.2_CO	CuO.MCF.6.2	MCF	30	6.2	CO reduction
MCF_8.9_CO	CuO.MCF.8.9	MCF	30	8.9	CO reduction
MCF_12.4_CO	CuO.MCF.12.4	MCF	30	12.4	CO reduction
MCF_18.7_CO	CuO.MCF.18.7	MCF	30	18.7	CO reduction
MCF_22.2_CO	CuO.MCF.22.2	MCF	30	22.2	CO reduction
MCM_18.7_CO	CuO.MCM.18.7	MCM-41	2	18.7	CO reduction
S15_18.7_CO	CuO.S15.18.7	SBA-15	8	18.7	CO reduction
S16_18.7_CO	CuO.S16.18.7	SBA-16	5	18.7	CO reduction
SG3_18.7_CO	CuO.SG3.18.7	SG3	3	18.7	CO reduction
SG6_18.7_CO	CuO.SG6.18.7	SG6	6	18.7	CO reduction
SG15_18.7_CO	CuO.SG15.18.7	SG15	15	18.7	CO reduction
SG23_18.7_CO	CuO.SG23.18.7	SG23	23	18.7	CO reduction

Cu₂O. For example MCF_18.7_CO stands for Cu₂O supported by MCF with 18.7 wt% of Cu which was obtained by CO reduction method. Table 1 shows an overview of the samples discussed in this paper.

2.3. Characterization

Nitrogen physisorption measurements were conducted at -196°C using a Micromeritics Tristar 3000 to study the pore structure of the supporting materials. The pore size distributions were determined from the adsorption isotherms by the BJH method and the window size distributions were determined from desorption isotherms by the BJH method. The total pore volume was taken as the single point pore volume at $P/P_0 = 0.95$. X-ray diffractometry (XRD) was carried out using a Bruker D2 phaser diffractometer using Cu-K $\alpha_{1,2}$ radiation with $\lambda = 1.5405\text{ \AA}$, operated at 30 kV. Measurements were carried out between $2\theta = 20^{\circ}$ and 70° using a step size of 0.05° and a scan speed of $0.5^{\circ}\text{ s}^{-1}$. XRD peak intensities were normalized to the peak area of the amorphous silica support between 20° and 30° . Subsequently for each sample the diffractogram of the corresponding bare silica support was subtracted to emphasize the properties of the supported nanocrystallites. The crystallite sizes of the obtained nanoparticles were calculated from XRD line broadening analysis.

Transmission electron microscopy (TEM) was performed in a Tecnai 20FEG (FEI) electron microscope equipped with an HAADF detector and a field emission gun with an EDAX Super Ultra Thin Window (SUTW) EDS detector. High-resolution transmission electron microscopy (HRTEM) was performed in a Talos F200x (FEI) transmission electron microscope equipped with a Ceta CCD camera. To be able to obtain accurate particle size distributions, supported nanoparticles were prepared by embedding the crushed sample in a two component epoxy resin (Epoxy, EMS) and cured at 60°C overnight. Subsequently the sample was cut into thin sections ($50\text{--}100\text{ nm}$) using a Diatome Ultra 35° diamond knife mounted on a Ultracut E microtome (Reichert-Jung) and collected on a TEM grid. Energy dispersive X-ray (EDX) spectroscopy was processed with Tecnai Imaging and Analysis software (TIA). Samples were emplaced on a carbon coated Ni TEM grid (Agar 162 200 Mesh Ni, Van Loenen instruments).

Temperature programmed reduction (TPR) was performed with Micromeritics ASAP2920, equipped with a TCD detector for H₂ reduction and a mass spectrometer (MS) for CO reduction. The samples ($\sim 100\text{ mg}$) were first dried in an argon flow at 120°C and then heated with a temperature ramping of $5^{\circ}\text{C}/\text{min}$ to a maximum temperature of 500°C in a quartz reactor under $50\text{ mL}/\text{min}$ of 5% CO/95% N₂ or 5% H₂/95% Ar gas flow.

Diffuse reflectance Ultraviolet-Visible spectroscopy spectra were collected using a Varian Cary 500 UV/Vis/NIR spectrometer

equipped with a diffuse reflectance spectroscopy (DRS) accessory using barium sulfate as the reflectance standard. Sample was placed in a cylinder reactor with 20 mm in diameter and 0.64 mm in depth. The spectra were collected between 300 and 800 nm with a data interval of 1 nm and at a rate of 600 nm min^{-1} . Using Kubelka-Munk function, $(\alpha h\nu)^2$ was plotted versus $h\nu$ (α : absorption coefficient, h : Planck's constant, ν : frequency of vibration) [25]. The direct optical band gap can be obtained from the intercept of the resulting straight lines with the energy axis at $(\alpha h\nu)^2 = 0$.

2.4. Photocatalytic hydrogen evolution

The performance of the as-obtained silica supported Cu₂O nanoparticles in the photo-reduction of H₂O to H₂ with and without methanol as the sacrificial electron donor was investigated in a 25 mL airtight reaction vessel with a quartz window and equipped with connections for inlet/outlet of argon gas (2 mL/min). H₂ evolution was examined from either 20 mL water or 1:1 (by volume) water-methanol mixture containing 0.02 g (weight of Cu₂O) of silica supported Cu₂O powder. After purging the solution to remove traces of oxygen, the reactor was irradiated at room temperature for 200 min with a 150 W Xenon lamp (Newport) equipped with a filter (Thorlabs) transmitted light between 310 nm and 710 nm, and calibrated with a Si diode (Thorlabs) to simulate AM1.5 illumination (100 mW cm^{-2}). A mask with an aperture of 0.785 cm^2 is used to define the whole illuminated surface area. The evolved gas was transported by 2 mL/min argon carrier gas to an online Gas Chromatography (GC, Shimadzu GC-2014) system, equipped with a porapack Q precolumn to retain water, a ShinCarbon ST 100/120 column for gas separation and a Thermal Conductivity Detector (TCD) for H₂ analysis.

External Quantum Efficiencies (η_{ext}) were calculated using the following equation:

$$\eta_{\text{ext}} = \int_{310\text{ nm}}^{710\text{ nm}} \frac{2 \times N_{\text{total}}}{n_p(\lambda)} d\lambda$$

where N_{total} is the amount of evolved H₂ molecules per second, which was obtained by the integration of the TCD signal of the GC; n_p is the number of incident photons within a specific wavelength range.

$$n_p(\lambda) = \frac{E_i(\lambda)}{E_p(\lambda)}$$

where $E_i(\lambda)$ is the incident power of the light (in W) over the whole illuminated surface area (0.785 cm^2), which was obtained by the integration of the lamp spectra between the wavelengths of 310 and 710 nm over 5 nm increments; photon energy $E_p = hc/\lambda$, where

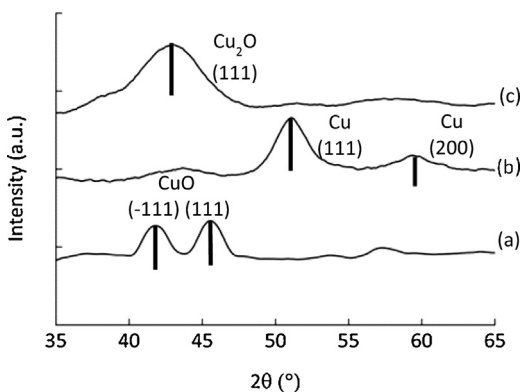


Fig. 1. XRD patterns of (a) 3 nm CuO@SiO₂ nanoparticles (CuO.ARS.10.0); (b) after reduction of CuO@SiO₂ nanoparticles in H₂ for 3 h, followed by reoxidation at room temperature, 3 nm Cu@SiO₂ nanoparticles with Cu₂O passivation layer are obtained (Cu.ARS.10.0); (c) after liquid phase oxidation of Cu@SiO₂ nanoparticles with chloroform, 3 nm Cu₂O@SiO₂ nanoparticles are obtained (ARS.10.0.CH). (curves offset to facilitate comparison).

λ is the wavelength of the median point in each 5 nm increment, h is the Planck constant and C is the speed of light in vacuum.

Internal Quantum Efficiencies (η_{int}) were calculated using the following equation:

$$\eta_{int} = \int_{310\text{nm}}^{710\text{nm}} \frac{2 \times N_{\text{total}}}{a_{\lambda} \times n_p(\lambda)} d\lambda$$

where a_{λ} is the fraction of the total incident energy that was absorbed by Cu₂O nanoparticles, which was obtained by the integration of the light absorption spectrum of the Cu₂O nanoparticles between the wavelengths of 310 and 710 nm over 5 nm increment.

3. Results and discussion

3.1. Overview

Silica gels with different pore diameters (SG3, SG6, SG15, and SG23) and ordered mesoporous silica MCM-41, SBA-16, SBA-15 and MCF were employed. The N₂ physisorption isotherms of these mesoporous silica supports are given in Fig. S1(a,b). A summary of the detailed textural properties of the silica materials is shown in Table S1. An overview of the CuO crystallite sizes after heat treatment, Cu crystallite size after reduction in H₂ and the as-obtained Cu₂O crystallite size are given in Table 2. It should be noted that it can be tricky to determine particle sizes in detail, especially when dealing with metal oxide, therefore we compared the XRD patterns of a single sample in fully reduced, partially oxidized and fully oxidized state (MCF supported CuO, Cu₂O and metallic Cu) in Fig. S1(c).

3.2. Liquid phase oxidation of Cu to Cu₂O

Ex-situ X-ray diffractometry (XRD) was used to examine the crystalline phase transformations of the nanoparticles. CuO nanoparticles supported by Aerosil 300 (CuO.ARS.10.0) were prepared via the impregnation-drying-heating. As shown in Fig. 1(a), the peaks from XRD measurement on the as-prepared sample correspond to the (−111) and (111) diffraction of CuO with an face-centered cubic (fcc) structure. The crystallite size was determined from the peak broadening using the Scherrer equation. The value of 3 nm corresponded to the pore diameter of the Aerosil 300 silica (3 nm). After reduction in H₂ for 3 h at 250 °C, the peaks in the XRD

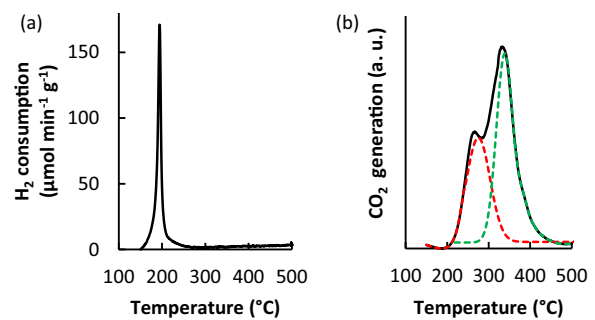


Fig. 2. Reduction of CuO.SG23.18.7 in (a) 5% H₂/95% Ar and (b) 5% CO/95% N₂ gas flow. (temperature ramping: 5 °C/min, flow rate: 50 mL/min).

pattern (Fig. 1(b)) are indexed to Cu with an fcc structure. A weak signal also shows up at around 42.5° which corresponds to the (111) diffraction of Cu₂O with an fcc structure, and which we tentatively assign to the formation of a passivation layer due to reaction with air.

We investigated oxidation of the Cu nanoparticles to Cu₂O nanoparticles. As Cu₂O is not a thermodynamically stable phase, we had to rely on kinetic control to stop the reaction at Cu₂O. To study the oxidation of Cu in organic solvent, we dispersed the Aerosil 300 supported Cu nanoparticles (3 nm crystallite size) in chloroform under ambient conditions. The solution was black immediately after dispersing the particles. The color gradually changed to dark green within 6 h and then turned yellow after 12 h. Fig. 1(c) shows that after 24 h of dispersion in chloroform the peaks of the Cu₂O phase had increased in intensity, whereas those of the Cu phase had disappeared, consistent with the formation of Cu₂O nanoparticles. The same approach was applied to CuO nanoparticles with larger crystallite sizes (16 nm on MCF, 18.7 wt% of Cu). XRD patterns (Fig. S2) of the resulting samples show the co-existence of a Cu₂O and metallic Cu phase. Hence with this method, the effectiveness to obtain pure Cu₂O depends on the Cu crystallite size [26].

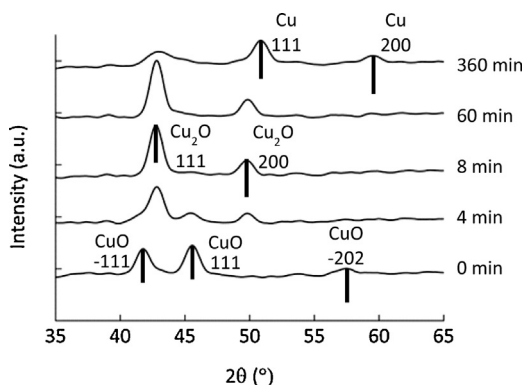
3.3. Gas phase reduction of CuO to Cu₂O

We compared H₂ and CO as gas-phase reducing agents for CuO. The reduction of 23 nm pore sized silica gel (SG23) supported CuO nanoparticles (CuO.SG23.18.7) was followed to see whether, and at which temperature, partial reduction to Cu₂O was possible. Fig. 2(a) shows the temperature programmed reduction profile with H₂ in which there is only one single reduction peak with a maximum at 192 °C. This suggests the direct conversion of CuO to metallic copper without the formation of a Cu₂O phase. It was reported by Hanson et al. that CuO nanoparticles were slowly reduced into Cu₂O by CO gas [27], hence reduction with carbon monoxide (CO) was investigated as an alternative. Fig. 2(b) shows the reduction of 10 nm CuO nanoparticles (CuO.SG23.18.7). Two peaks with maxima at 261 °C and 331 °C were observed. This suggests that the gas phase reduction of CuO with CO is a two-step process in contrast with H₂. It suggested that CuO was converted into Cu₂O at first, further reduction into Cu started at around 280 °C. Hence using CO as a reduction agent seems promising to attain Cu₂O nanoparticles. The CO reduction profile in Fig. 2(b) suggested that the Cu₂O phase was formed between 200 °C and 300 °C, hence we investigated isothermal reduction. The 10 nm CuO nanoparticles (CuO.SG23.18.7) were reduced under 5% CO/95% N₂ gas at 250 °C. XRD (Fig. 3) shows that within 4 min of reduction at 250 °C, the (−111) and (111) diffractions of 10 nm CuO nanoparticles have mostly disappeared, and the (111) diffraction of 10 nm Cu₂O has appeared. The Cu₂O phase was stable while holding at 250 °C for up to 60 min. Cu₂O was partially reduced further into Cu when the reduction time was extended to

Table 2

Overview of crystallite sizes of samples (calculated from XRD line broadening analysis).

sample name (after CO/H ₂ /CH ₃ Cl) treatment	sample name of Cu(O)	size of Cu or CuO (nm)	size of Cu ₂ O (nm)
ARS_10.0_CH	Cu.ARS_10.0	3	3
ARS_10.0_CO	CuO.ARS_10.0	3	3
MCF_18.7_CH	Cu.MCF.18.7	16	–
MCF_6.2_CO	CuO.MCF.6.2	3	3
MCF_8.9_CO	CuO.MCF.8.9	6	5
MCF_12.4_CO	CuO.MCF.12.4	8	8
MCF_18.7_CO	CuO.MCF.18.7	16	15
MCF_22.2_CO	CuO.MCF.22.2	15	15
MCM_18.7_CO	CuO.MCM.18.7	2	2
S15_18.7_CO	CuO.S15.18.7	6	5
S16_18.7_CO	CuO.S16.18.7	3	3
SG3_18.7_CO	CuO.SG3.18.7	4	4
SG6_18.7_CO	CuO.SG6.18.7	6	6
SG15_18.7_CO	CuO.SG15.18.7	7	7
SG23_18.7_CO	CuO.SG23.18.7	10	10
SG23_18.7_H ₂	CuO.SG23.18.7	10	–

**Fig. 3.** XRD patterns of CuO.SG23.18.7 and after reduction under 5% CO/95% N₂ at 250 °C for different times. (curves offset to facilitate comparison).

6 h. Hence, in CO, the crystalline part of CuO can be reduced to Cu₂O before significant further reduction to metallic copper occurs.

The same reduction method was applied to CuO supported on ordered mesoporous silica. 16 nm CuO nanoparticles supported by MCF (CuO.MCF.18.7), which were obtained by impregnation-drying-heating, were reduced under 5% CO/95% N₂ gas flow at 250 °C for 30 min, and 15 nm Cu₂O nanoparticles (MCF_18.7_CO) were obtained. The gas phase reduction method with CO proves robust and applicable to larger crystallite sizes. This mild reduction method is also suitable to prepare other metal oxide materials with intermediate valency, e.g. 10 nm CoO on MCF was obtained after the reduction of 12 nm Co₃O₄ under 5% CO/95% N₂ gas at 250 °C for 15 min.

3.4. Characterization of the supported Cu₂O nanoparticles

As an example we show the detailed characterization of sample MCF_18.7_CO. The transmission electron micrograph (TEM) of an ultramicrotome section of the samples (Fig. 4(a–c)) shows the presence of nanoparticles in the silica pores. The distribution of those nanoparticles over the MCF support seems more homogeneous than over the other kinds of supports [16,17,19], which is caused by the unique 3-D pore system and relatively large pore volume of MCF. Energy-dispersive X-ray spectroscopy (EDX) analysis confirmed that these nanoparticles contained Cu (Fig. S3). Analysis of the particle size (Fig. 4(d)) shows that the number-averaged particle size is 13.5 nm ± 4.0 nm. The conversion from CuO to Cu₂O did hence not significantly change the crystallite size (from 16 nm of CuO to 15 nm of Cu₂O based on XRD) or distribution (Fig. S4). The size histogram shows a bimodal distribution: about 6% of the

nano particles possess much larger particle sizes (20 nm–26 nm) than the others (6 nm–18 nm). One possible reason for this is that some of the nanoparticles aggregated and formed clusters with large crystallite size in the 30 nm pores of MCF during heat treatment.

HRTEM was used to further investigate the conversion of CuO to Cu₂O. Fig. 4(e) and (f) shows HRTEM images of the sample before and after reduction (CuO.MCF.18.7 and MCF_18.7_CO). The lattice fringes demonstrate that the particles are highly crystalline. The diffraction patterns are shown as insets. The 2.51 Å and 2.36 Å lattice fringes seen in Fig. 4(e) correspond to the reflections from the (–111) and (111) planes of CuO (PDF 04-007-0518). The 2.96 Å, 2.43 Å and 2.13 Å lattice fringes seen in Fig. 4(f) correspond to the reflections due to the (110), (111) and (200) planes of Cu₂O (PDF 04-007-9767). We observe no diffraction spots corresponding to metallic Cu (2.08 Å for the (111) plane and 1.81 Å for the (200) plane, PDF 00-004-0836). Those results confirm that upon CO reduction, CuO crystallites were converted into Cu₂O crystallites.

Optical absorption spectra are shown in Fig. 5. Before reduction, the material (CuO.MCF.18.7) absorbs a large fraction of visible light below 650 nm, while after reduction, the onset wavelength of absorption is shifted to 530 nm. This confirms the conversion from CuO to Cu₂O nanoparticles which have a larger band gap. As shown in Fig. 5(b), plotting $(\alpha h\nu)^2$ vs. $h\nu$ (α : absorption coefficient, h : Planck's constant, ν : frequency of vibration) [28] indicates a direct band gap energy of 2.15 eV and 2.53 eV for CuO and Cu₂O, respectively. Compared to the band gap of macrocrystalline Cu₂O (1.94 eV), our Cu₂O nanoparticle samples show a wider optical bandgap.

3.5. Cu₂O with tunable crystallite size and variable band gap

We explored two strategies to tune the Cu₂O crystallite size. One way to obtain supported Cu₂O nanoparticles with different crystallite sizes is to prepare the nanoparticles using mesoporous silica with different pore sizes. Another strategy is to adjust the concentration of Cu(NO₃)₂ precursor solutions to obtain MCF supported CuO nanoparticles with different weight loadings.

Fig. 6(a) shows the effect of the silica support pore size on the Cu₂O crystallite size. With increasing pore diameter of the supporting silica (from 2 nm to 30 nm), increasing Cu₂O crystallite sizes after calcination and reduction (from 2 nm to 16 nm) were obtained. Previous work by our group has already shown that the crystallite size of Cu cannot be tuned by varying the weight loading when using small pore materials as supports [17], so in the present work we used large pore MCF with 30 nm pore diameter as the support. The weight loading was varied by varying the concentration of the

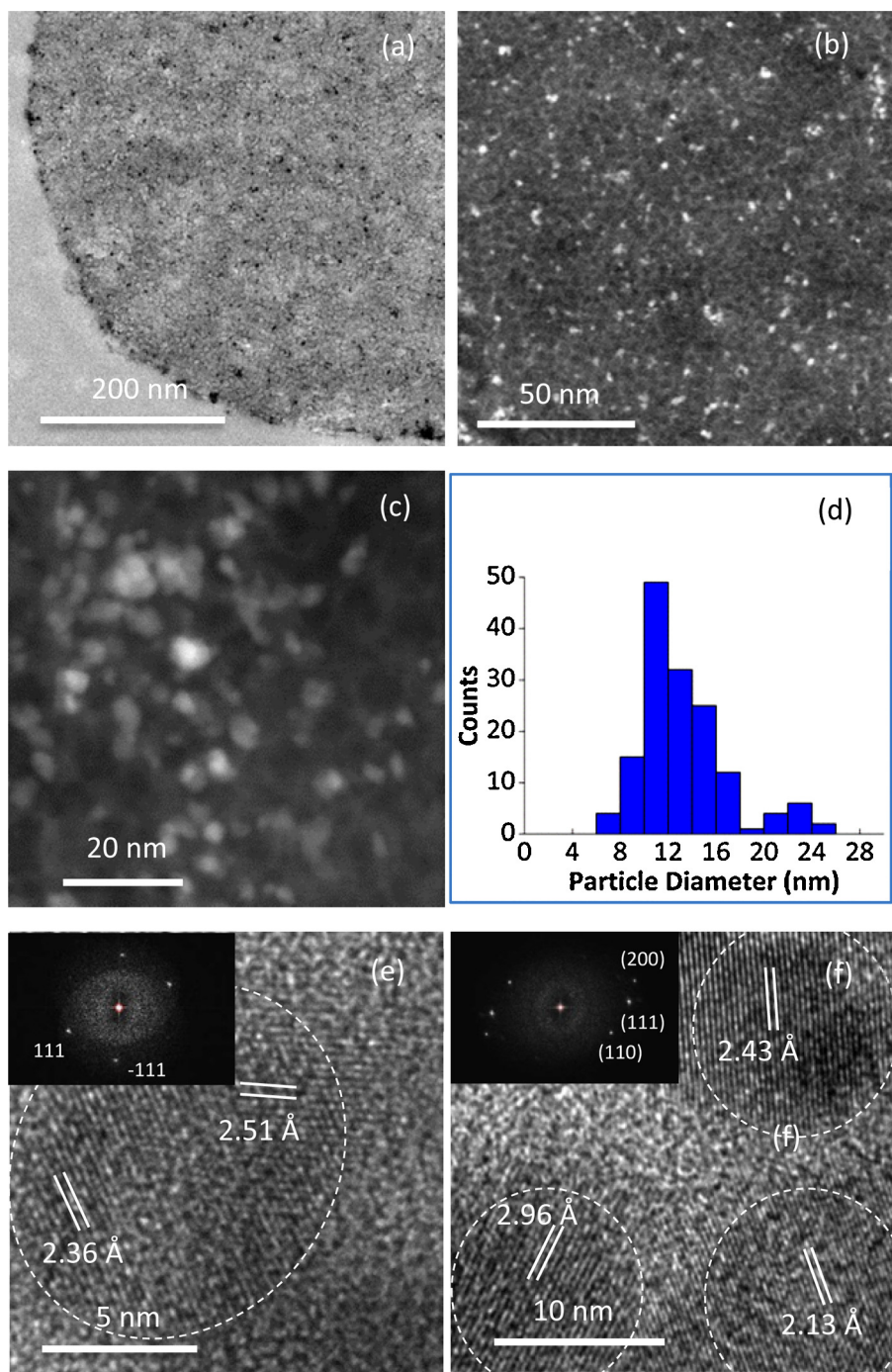


Fig. 4. (a) Bright-field TEM image and (b) (c) HAADF-STEM images of the cross section of Cu_2O supported by MCF (MCF_18.7.CO) and (d) corresponding particle size histogram; HRTEM images (diffraction patterns added as insets) of (e) sample before CO reduction (CuO_MCF_18.7) and (f) after CO reduction (MCF_18.7.CO), showing the lattice fringes corresponding to the (-111) and (111) planes of CuO and the (110) , (111) and (200) planes of Cu_2O .

Table 3

Overview of the performance of Cu_2O nanoparticles in hydrogen evolution reaction.

Cu_2O	Crystallite size (nm)	H_2 evolution rate at 110th min ($10^{-3} \mu\text{mol min}^{-1}$)	Corresponding internal quantum efficiency (%)	H_2 evolution rate at 180th min ($10^{-3} \mu\text{mol min}^{-1}$)
MCF_6.2.CO	3	4.5	6.3	4.4
MCF_8.9.CO	5	4.2	6.2	3.8
MCF_12.4.CO	8	7.9	11.0	7.2
MCF_18.7.CO	15	11.5	15.8	10.4
macrocrystalline Cu_2O	~ 4000	0	0	0

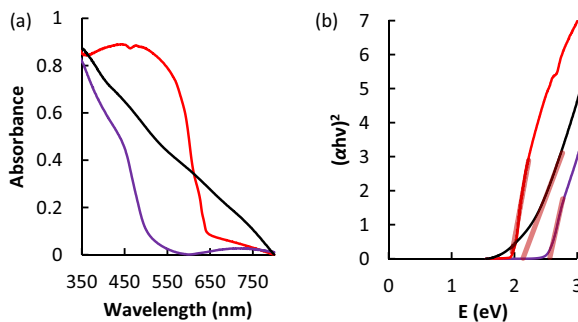


Fig. 5. (a) The optical absorption spectra of CuO_MCF_18.7 (1), MCF_18.7.CO (2) nanoparticles and 4 μm sized macrocrystalline Cu₂O (3) plotted versus wavelength (b) and $(\alpha h\nu)^2$ versus the photo energy E.

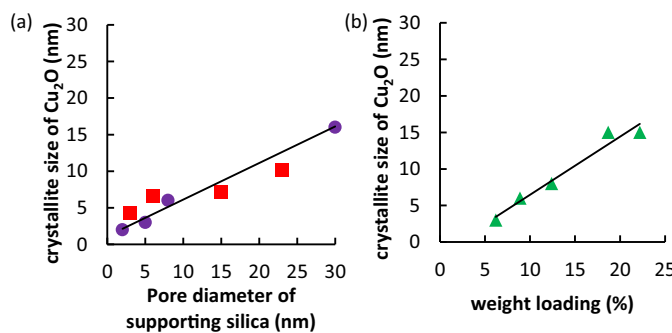


Fig. 6. Influence of (a) pore diameter of the supporting silica (18.7% weight loading of Cu, square: supported on silica gel; circle: supported on MCM-41, SBA-16, SBA-15, MCF (from left to right)) and (b) weight loading on the Cu₂O crystallite size.

Cu(NO₃)₂ precursor solution from 0.5 M to 2.5 M. With the increase of weight loading (6.2%, 8.9%, 12.4%, 18.7%, 22.2%) of copper on MCF, gradually increasing Cu₂O crystallite sizes after heat treatment and reduction in CO (3 nm, 6 nm, 8 nm, 15 nm, 15 nm) were obtained (Fig. 6(b)).

Although both strategies work, obtaining different size nanocrystals by changing the pore diameter of the supports has the advantage of changing the crystallite size while shown in Table 1. The resulting crystallite size increases continuously with the increase of pore diameter of the supports. However, for MCF supported particles, their crystallite size (~15 nm) is much smaller than the MCF pore size (30 nm). This can be explained by the fact that the concentration of the Cu(NO₃)₂ precursor solution is limited between 0.5 M and 2.5 M and therefore, after the drying procedure, the Cu(NO₃)₂ left in the supports is not enough to fill the pores. For example, after drying a 2.0 M precursor solution can only fill 26% of the pore volume of MCF with 30 nm diameter pores.

Fig. 7 shows the optical absorption spectra of silica gel supported Cu₂O nanoparticles in the UV-vis region. The absorption between 350 nm and 550 nm is assigned to the band-to-band transition in nanocrystalline Cu₂O. A broad feature centered at around 700 nm is also observed, and becomes more pronounced with decreasing crystallite size. This band may be assigned to a plasmon resonance. Localized surface plasmon resonances (LSPRs) are commonly observed in copper(I) chalcogenide nanoparticles, since these materials can easily accommodate significant concentrations of Cu vacancies, which introduce free carriers (holes) in the valence band. The hole density in Cu_{2-x}A (A=S, Se, Te) nanocrystals may become sufficiently high to sustain LSPRs, which depends not only on the composition of the nanocrystal, but also on their size and shape [29]. The direct band gap is determined by plotting $(\alpha h\nu)^2$ vs. $h\nu$ and extrapolating the linear fitted regions to $(\alpha h\nu)^2 = 0$. In general, a shift in the absorption towards higher energy with a

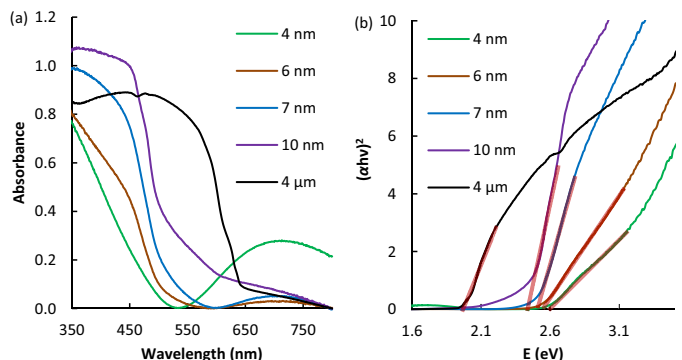


Fig. 7. The optical absorption spectra of Cu₂O nanoparticles on silica gel plotted versus wavelength (a) and $(\alpha h\nu)^2$ versus the photo energy E (b).

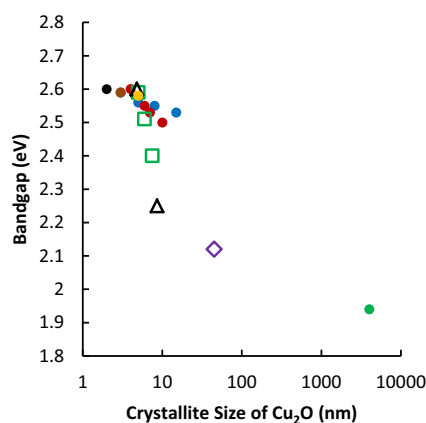


Fig. 8. The relationship between crystallite size and band gap of Cu₂O. (Closed symbols: our present results, red: 4–10 nm @ Silica gel, blue: 3–15 nm @ MCF, black: 2 nm @ MCM-41, brown: 3 nm @ SBA-16, yellow: 5 nm @ SBA-15, green: 4 μm sized macrocrystalline Cu₂O; Open symbols: data from literature, square: 5–7.5 nm, Banerjee et al., triangle: 9 nm, Knözinger et al., rhombus: 45 nm, Borgohain et al.). (For interpretation of the references to colour in this figure legend, the reader is referred to the web version of this article.)

decrease in size of the nanocrystals is observed. Fig. 8 shows that the observed Cu₂O band gaps decrease from 2.60 eV to 2.50 eV with an increase in crystallite size from 2 nm to 15 nm. The optical absorption spectra of bare silica supports and MCF supported Cu₂O nanoparticles are given in Figs. S5 and S6.

The band gaps reported in the literature for Cu₂O nanoparticles prepared by colloidal methods [30–32] are much smaller than those observed in the present work for similarly sized particles (Fig. 8). This difference may be attributed to a larger concentration of Cu vacancies in the nanoparticles prepared in this work. As discussed above, Cu vacancies introduce charge carriers (holes) in the material, giving rise to a plasmon resonance. This also effectively increases the band gap since the excess holes will occupy the top of the valence band (Moss-Burstein effect) [29,33]. Our results show that the optical properties of Cu₂O nanocrystals are related to crystallite size, which has a stronger impact on the absorption strength than on the bandgap. In general, semiconductor nanoparticles have an enlarged band gap when their size becomes comparable to or smaller than their exciton Bohr radius [11]. For Cu₂O, the exciton Bohr radius is 0.7 nm, [34,35] which excludes the possibility of quantum confinement effects for particles in the size range shown in Fig. 8. The modest size dependence observed for the band gaps of the Cu_{2-x}O nanocrystals prepared in the present work (100 meV in 2 nm–15 nm size range, Fig. 8) can thus be assigned to an increase in the concentration of Cu vacancies with decreasing crystallite size, possibly due to the increase in the surface to volume ratio.

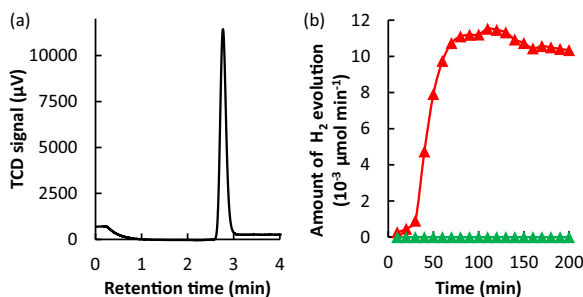


Fig. 9. (a) Gas chromatography of H_2 after irradiation for 110 min in 1:1 water-methanol mixture (sampling from 1 mL gas mixture); (b) Production of H_2 from 1:1 water-methanol mixture in the presence of Cu_2O (Red symbols: MCF-18.7.CO; green symbols: 4 μm sized macrocrystalline Cu_2O). (For interpretation of the references to colour in this figure legend, the reader is referred to the web version of this article.)

3.6. Photocatalytic hydrogen evolution

In pure water, no H_2 evolution was detected by gas chromatography (GC) in the presence of 15 nm Cu_2O @MCF (MCF-18.7.CO) under light illumination. Also in a 1:1 water-methanol mixture, no H_2 evolution was observed in the presence of MCF without Cu_2O upon illumination with light. And no H_2 was observed during 200 min of light illumination when 4 μm sized macrocrystalline Cu_2O was used as catalyst instead of Cu_2O nanoparticles. In a 1:1 water-methanol mixture, evolution of H_2 was detected when 15 nm Cu_2O @MCF nanoparticles were used as catalysts (Fig. 9(a)). Fig. 9(b) shows the time dependence of the H_2 evolution rate. No noticeable H_2 evolution was observed during the first 30 min of light illumination, this can be explained by a combination of two factors. Firstly, it would take about two minutes for the mixture of argon carrier gas and evolved H_2 to flush the dead volume of the tubing from the reactor towards the GC. Secondly, the solubility of H_2 in methanol is relatively large (0.8 mol m^{-3} in water and 3.9 mol m^{-3} in methanol at 25 °C and 1 atm [36]), part of the evolved H_2 molecules (about 0.55 μmol if we assume the catalytic activity achieved maximum immediately after light illumination) stayed in the mixture during the first hour of light illumination.

The external and internal quantum efficiencies at the point of maximum H_2 evolution were 3.5% and 15.8%, respectively, along with a H_2 evolution rate of $11.5 \times 10^{-3} \mu\text{mol min}^{-1}$. Hara et al. have reported a quantum efficiency of ca. 0.3% for the wavelength region of 550 and 600 nm when Cu_2O was used as a catalyst for photocatalytic splitting of pure water. Our results showed that the quantum efficiency was increased dramatically by adding sacrificial electron donor, hence the hole scavenging is the rate-limiting factor [6,37]. The hydrogen evolution rate reaches a maximum after about 100 min. The catalysts were retrieved after reaction and examined by XRD (Fig. S7), there was no significant change in terms of copper oxide phase and crystallite size.

An overview of the performance of Cu_2O crystallites with different sizes during hydrogen evolution is given in Table 3. The internal quantum efficiencies at the 110th min of light illumination for 3 nm, 5 nm, 8 nm and 15 nm Cu_2O were 15.8%, 11.0%, 6.2% and 6.3%, respectively. The generally decreasing efficiency with decreasing crystallite size is probably due to the higher electron-hole recombination rates for smaller nanoparticles. Recombination is mediated by defects and impurities, which are present at higher concentration at the surface [11], hence the high specific surface areas of smaller Cu_2O nanoparticles induce lower efficiencies for H_2 generation. All of the MCF supported samples were reasonably stable with a loss of ~10% in activity during the 180 min of photocatalysis.

4. Conclusions

CuO nanoparticles with crystallite sizes of 2 nm–16 nm were obtained by impregnating porous silica with a precursor solution, followed by drying and heating. Subsequently the CuO was converted into Cu_2O by liquid phase and gas phase reduction. Selective formation of Cu_2O was achieved via gas-phase reduction under CO in contrast to H_2 reduction. Careful tuning of conditions allowed us to attain a crystallite Cu_2O phase starting from either Cu or CuO . Cu_2O nanocrystallites with tunable size from 2 nm to 15 nm were obtained by the reduction of CuO of different particle size with CO at 250 °C. The reduction temperature and duration were critical for the generation of Cu_2O instead of a mixture of Cu_2O and metallic copper. The crystallite size was tuned either by varying the pore size of the support or by varying the weight loading of Cu in supports with large pore diameters. The optical properties of Cu_2O nanoparticles depended on the crystallite size, leading to an effective band gap of 2.60 eV for SiO_2 supported 2 nm crystallites compared to 1.94 eV for macrocrystalline Cu_2O . This new strategy for the preparation of supported semiconductor nanoparticles facilitates attaining differently sized photoactive nanoparticles, allowing the study of how crystallite size affects the catalytic activity and stability in photocatalytic systems. These Cu_2O nanoparticles showed relatively high activity and stability for photocatalytic water reduction in the 1:1 water-methanol mixture.

Acknowledgements

The research was financed by the Dutch National Research School Combination Catalysis Controlled by Chemical Design (NRSC-Catalysis). The authors would like to thank Hans Meeldijk, Marjan Versluijs and Dr. Rafael de Lima Oliveira for their helps with TEM measurements, XRD measurements and N_2 -physisorption measurements, respectively.

Appendix A. Supplementary data

Supplementary data associated with this article can be found, in the online version, at <http://dx.doi.org/10.1016/j.apcatb.2016.03.044>.

References

- [1] A. Fujishima, K. Honda, *Nature* 238 (1972) 37–38.
- [2] F.E. Osterloh, *Chem. Mater.* 20 (2008) 35–54.
- [3] A. Kudo, Y. Miseki, *Chem. Soc. Rev.* 38 (2009) 253–278.
- [4] G. Nagasubramanian, A.S. Gioda, A.J. Bard, *J. Electrochem. Soc.* 128 (1981) 2158–2164.
- [5] J. Ghijsen, L.H. Tjeng, J. van Elp, H. Eskes, J. Westerink, G.A. Sawatzky, *Phys. Rev. B* 38 (1988) 11322–11330.
- [6] M. Hara, T. Kondo, M. Komoda, S. Ikeda, K. Shinohara, A. Tanaka, Ju.N. Kondo, K. Domen, *Chem. Commun.* 3 (1998) 357–358.
- [7] A. Paracchino, V. Laporte, K. Sivula, M. Grätzel, E. Thimsen, *Nat. Mater.* 10 (2011) 456–461.
- [8] Z. Zhang, R. Dua, L. Zhang, H. Zhu, H. Zhang, P. Wang, *ACS Nano* 7 (2013) 1709–1717.
- [9] A. Paracchino, N. Mathews, T. Hisatomi, M. Stefik, S.D. Tilley, M. Grätzel, *Energy Environ. Sci.* 5 (2012) 8673–8681.
- [10] M. Yin, C. Wu, Y. Lou, C. Burda, J.T. Koberstein, Y. Zhu, S. O'Brien, *J. Am. Chem. Soc.* 127 (2005) 9506–9511.
- [11] C. de Mello Donega, *Chem. Soc. Rev.* 40 (2011) 1512–1546.
- [12] L. Gou, C.J. Murphy, *Nano Lett.* 3 (2003) 231–234.
- [13] Q. Hua, D. Shang, W. Zhang, K. Chen, S. Chang, Y. Ma, Z. Jiang, J. Yang, W. Huang, *Langmuir* 27 (2011) 665–671.
- [14] A. Gallo, T. Tsoncheva, M. Marellia, M. Mihaylov, M. Dimitrov, V. Dal Santo, K. Hadjivanov, *Appl. Catal. B: Environ.* 126 (2012) 161–171.
- [15] T. Toupane, M. Kermarec, C. Louis, *J. Phys. Chem. B* 104 (2000) 965–972.
- [16] P. Munnik, M. Wolters, A. Gabrielson, S.D. Pollington, G. Headdock, J.H. Bitter, P.E. de Jongh, K.P. de Jong, *J. Phys. Chem. C* 115 (2011) 14698–14706.
- [17] G. Prieto, J.D. Meeldijk, K.P. de Jong, P.E. de Jongh, *J. Catal.* 303 (2013) 31–40.
- [18] G. Prieto, J. Zecevic, H. Friedrich, K.P. de Jong, P.E. de Jongh, *Nat. Mater.* 12 (2013) 34–39.

[19] R. van den Berg, T.E. Parmentier, C.F. Elkjær, C.J. Gommes, J. Sehested, S. Helveg, P.E. de Jongh, K.P. de Jong, *ACS Catal.* 5 (2015) 4439–4448.

[20] P. Munnik, P.E. de Jongh, K.P. de Jong, *Chem. Rev.* 115 (2015) 6687–6718.

[21] P. Schmidt-Winkel, W.W. Lukens Jr., P. Yang, D.I. Margolese, J.S. Lettow, J.Y. Ying, G.D. Stucky, *Chem. Mater.* 12 (2000) 686–696.

[22] A. Sayari, B. Han, Y. Yang, *J. Am. Chem. Soc.* 126 (2004) 14348–14349.

[23] O.C. Gobin, Y. Wan, D. Zhao, F. Kleitz, S. Kaliaguine, *J. Phys. Chem. C* 111 (2007) 3053–3058.

[24] Q. Cai, Z. Luo, W. Pang, Y. Fan, X. Chen, F. Cui, *Chem. Mater.* 13 (2001) 258–263.

[25] G. Kortüm, W. Braun, G. Herzog, *Angew. Chem. Int. Ed.* 2 (1963) 333–341.

[26] L. Hung, C. Tsung, W. Huang, P. Yang, *Adv. Mater.* 22 (2010) 1910–1914.

[27] J. Pike, S. Chan, F. Zhang, X. Wang, J. Hanson, *Appl. Catal. A: Gen.* 303 (2006) 273–277.

[28] L. Wang, K. Han, M. Tao, *J. Electrochem. Soc.* 154 (2007) D91–D94.

[29] W. van der Stam, A.C. Berends, C. de Mello Donega, *ChemPhysChem* 17 (2016) 559–581.

[30] K. Borgohain, N. Murase, S. Mahamuni, *J. Appl. Phys.* 92 (2002) 1292–1297.

[31] S. Banerjee, D. Chakravorty, *Europhys. Lett.* 52 (2000) 468.

[32] E. Knözinger, A. Kellersohn, W. Langel, M. Giersig, *Adv. Mater.* 7 (1995) 652–655.

[33] Y. Zhao, H. Pan, Y. Lou, X. Qiu, J. Zhu, C. Burda, *J. Am. Chem. Soc.* 131 (2009) 4253–4261.

[34] K. Borgohain, N. Murase, S. Mahamuni, *J. Appl. Phys.* 92 (2002) 1292–1297.

[35] G.M. Kavoulakis, Y. Chang, G. Baym, *Phys. Rev. B* 55 (1997) 7593–7599.

[36] K. Radhakrishnan, P.A. Ramachandran, P.H. Brahme, R.V. Chaudhari, *J. Chem. Eng. Data* 28 (1983) 1–4.

[37] D. Barreca, P. Fornasiero, A. Gasparotto, V. Gombac, C. Maccato, T. Montini, E. Tondello, *ChemSusChem* 2 (2009) 230–233.